Materials Science

Volume 2, Issue 3, 260-278.
DOI: 10.3934/matersci.2015.260
Received date 31 May 2015,
Accepted date 16 August 2015,
Published date 21 August 2015

http://www.aimspress.com/

Research article

Concurrent interface shearing and dislocation core change on the glide dislocation-interface interactions: a phase field approach

Songlin Zheng, Yong Ni *, and Linghui He

CAS Key Laboratory of Mechanical Behavior and Design of Materials, and Department of Modern Mechanics, University of Science and Technology of China, Hefei, Anhui, 230026, P. R. China

*** Correspondance:** E-mail: yni@ustc.edu.cn.

Abstract: Strengthening in nanoscale metallic multilayers is closely related to the glide dislocation-interface interaction. The interface can be sheared by the stress of the approaching glide dislocation with its core changed. How the concurrent interface shearing and the dislocation core change influence such interaction dominated strength is studied using three dimensional phase field microelasticity modeling and simulation. The simulated results show that when the glide dislocation is close to or away from the interface, the width of its core changes abruptly in accompany with the interface shear zone broadening or shrinking, respectively. A wider interface shear zone is developed on the interface with a lower shear strength, and can trap the glide dislocation at the interface in a lower energy state, and thus leads a stronger barrier to dislocation transmission. The results further show that the continuum model of the dislocation without the core-width change underestimates the interfacial barrier strength especially for the glide dislocation transmission across weak interfaces.

Keywords: strength; metallic multilayer; phase field; dislocation; interface shear

1. Introduction

Computer modeling and simulation of defects ensemble and their elastic interactions from atomistic scale to continuum scale are important to get insights into mechanism-based strength or plasticity in materials [1,2]. Especially computational modeling capable of bridging multiple time and length scales becomes one of the fast growing areas in understanding the mechanical response of materials [3]. In metallic multilayers, the strength shows a maximum at a critical layer thickness [4–7]. The maximum is closely related to the critical stress required to transmit a glide

dislocation across an interface wherein the interface acts as a barrier to impede the movement of the dislocation [7–9]. How the interfacial properties influence on the interfacial barrier strength has been widely studied by theoretical [10–18] and atomistic models [19–26].

Shen and Anderson [16,17] study the interfacial barriers of both welded (non-slipping) and slipping interface. Their results predict that significant interfacial sliding delocalizes the dislocation core within the slipping interface and creates a larger barrier to slip transmission in comparison with the welded interface. By using atomistic modeling, Rao and Hazzledine [20] show that screw dislocations in Cu prefer to spread on the Cu-Ni interface rather than to transmit into Ni. The molecular dynamics simulations performed by Hoagland et al. [21] indicate that opaque interfaces composed of two different crystal structures (e.g., Cu-Nb) present larger barrier strength than transparent interfaces with nearly continuous slip systems (e.g., Cu-Ni). The atomistic simulation results given by Wang et al. [22–24] demonstrate that these opaque interfaces with low shear strength ("weak" interfaces) exhibit strong barrier. They also show that the slip transmission barrier calculated by the chain of states method increases with the decrease of the interface shear strength [25]. By using the Green function method for anisotropic bimaterials, Chu et al. [18] employ dislocation-based interface shear models to systematically discuss the dislocation-interface interaction for possible implementation into large scale dislocation dynamic simulations. These models suggest that the interface shear results in an attractive force to trap the glide dislocation at the interface and thus leads to a barrier to dislocation transmission.

The force on the glide dislocation exerted by the interface is attractive only if the total energy increases as the glide dislocation is away from the interface. The maximum attractive force that should be overcome by the external stress can be viewed as the interfacial barrier strength during the dislocation escaping from the interface. Recent atomistic simulations further indicated that the interface shear involves the nucleation and growth of interfacial dislocations, and there is indeed an abrupt energy decrease like an energy well when the glide dislocation approaches the interface [21–25]. The weaker interface in shear shows a wider glide dislocation core spreading, results in a deeper energy drop at the interface, and produces a larger attractive force and thus a stronger interfacial barrier strength for slip transmission [25]. The energy decrease is significantly influenced by both the dislocation line energy change due to the core spreading [16], and the complicated cross-slip interaction between the glide dislocation and the induced interfacial dislocations [25]. Their contributions to the interfacial barrier strength are not additive due to the nonlinear coupling wherein the dislocation core change adaptively counteracts the stress concentration induced by the glide dislocation and the induced interfacial dislocations.

Developing a continuum model taking into account concurrent interface shearing and dislocation core change to reproduce the energy change during the glide dislocation across the interface is useful. In contrast to the dislocation-based interface shear model wherein the dislocations are described as line defects with compact cores, phase field model of dislocations could describe arbitrary dislocation core configurations, elastic interactions between arbitrary dislocations coupled with external applied stress [27–36]. After incorporating the stacking fault energy (SFE) of the shearable interface into the PFM model, similar to the case of γ-surface [30,32,37], a phase field approach could be applied to study the glide dislocation-interface interaction [36]. In addition different relaxation rate constants in the phase field model could characterize different dislocation mobilities on the glide plane and the interface, the rate competition between the transmission

processes and the interface shearing process can be addressed as well [36]. In this paper such phase field approach is adopted to discuss the effect of concurrent interface shearing and dislocation core change on the interfacial barrier strength for the glide dislocation transmission. It is worth to mention that recently the large-deformation phase field theory is developed and applied for the interaction between dislocations and phase interfaces [38–44]. The important mechanism of interface motion elucidated by this improved model is enlightening for dislocation-interface interaction. Although in the current study we use the small-deformation phase field model, and these calculations are not yet material specific because the simple stacking fault energy surfaces for the glide plane and the interface are adopted. It would provide valuable trend in what determines the width and depth of the energy well, the interfacial barrier strength for slip transmission and give insight into the limitations of continuum model of the dislocation without the core-width change.

2. Phase Field Model of the Glide Dislocation Across a Coherent Sliding Interface

In the current model we consider a screw dislocation across a bi-material coherent interface shown in Figure 1. The glide plane is denoted by $z=0$ and the interface between phases I and II is viewed as a mathematically sharp plane denoted by $x=0$. To focus on the effects of the concurrent interface shearing and the dislocation core change, the lattice mismatch between the two phases is ignored. A pre-existing dislocation at the glide plane in phase II tends to glide across the interface under an external shear, σ_{yz}^{ext}. The straight glide dislocation with the Burgers vector and the line direction both parallel to y axis is assumed to be a pure screw type for simplicity, the resultant shear

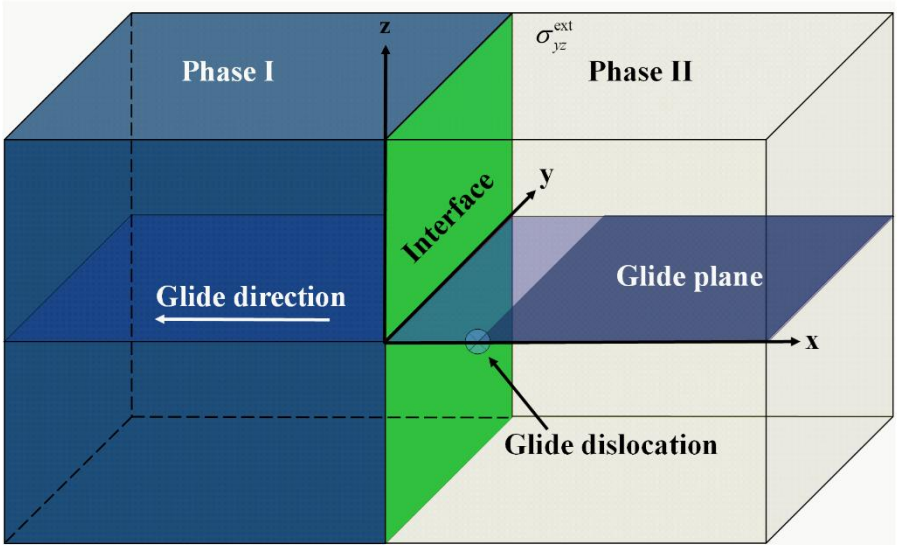

Figure 1. Sketch of a glide dislocation approaching a bimaterial interface under an applied shear stress.

stress by the dislocation only has the component along y axis, and thus the stress-driven nucleated interfacial dislocation only includes pure screw component. Because the initial glide dislocation is straight and the external stress is pure shear, the glide dislocation and the nucleated interfacial dislocation keep straight and pure screw all the time. We adopted a 3D PFM model to treat the interplay between the dislocation glide and the movement of interfacial dislocations. In the PFM modeling [27], the phase field variables $\eta(\alpha, m_\alpha, \mathbf{r})$ are used to represent the amount of relative slips in the slip plane α and the slip direction m_α in units of the Burgers vector $\mathbf{b}(\alpha, m_\alpha)$. The evolution of $\eta(\alpha, m_\alpha, \mathbf{r})$ characterizes the dislocation assembly towards equilibrium, driven by minimizing the total system free energy including the crystalline energy E^{cryst} caused by localized slips, their elastic interaction energies E^{elas} and the additional energy E^{ext} induced by applied stress

$$E^{\text{tot}} = E^{\text{cryst}} + E^{\text{elas}} + E^{\text{ext}}. \tag{1}$$

The gradient term included in the original PFM models [27] is removed here for simplicity followed by the previous work [32,33,36].

Here two phase field variables, $\eta^{\text{s}}(\mathbf{r})$, $\eta^{\text{int}}(\mathbf{r})$ are introduced as shape functions of the slipped regions. $\eta^{\text{s}}(\mathbf{r}) = 1$ and $\eta^{\text{int}}(\mathbf{r}) = 1$ are in the slipped area at the glide plane and the interface respectively, while $\eta^{\text{s}}(\mathbf{r}) = 0$ and $\eta^{\text{int}}(\mathbf{r}) = 0$ are in the unslipped area at the glide plane and the interface respectively. Following the treatment in the PFM, formulating the total free energy in Eq.(1) as a function of the two phase fields can be obtained. The crystalline energy (interplanar potential energy) caused by localized slip is given by

$$E^{\text{cryst}} = \int \sum_{\alpha, m_\alpha} \Phi\left[\mathbf{\Delta}(\alpha, m_\alpha, \mathbf{r})\right] \mathrm{d}^3 r, \tag{2}$$

where Φ is the density of interplanar potential energy as a functional of the interplanar slip $\mathbf{\Delta}(\alpha, m_\alpha, \mathbf{r})$ (the relative shear displacement) in the slip plane α and slip direction m_α. In Rice's model [44], the expression of Φ in terms of the total interplanar slip $\mathbf{\Delta}(\alpha, m_\alpha, \mathbf{r})$ has the form

$$\Phi = \frac{\gamma(\alpha, m_\alpha)}{d(\alpha)} \sin^2\left[\pi \frac{\mathbf{\Delta}(\alpha, m_\alpha, \mathbf{r})}{\mathbf{b}(\alpha, m_\alpha, \mathbf{r})}\right], \tag{3}$$

where $\gamma(\alpha, m_\alpha)$ is the unstable SFE in the slip plane α and slip direction m_α, $d(\alpha)$ is the interplanar distance of slip plane α, and then the interplanar shear stress is defined as

$$\boldsymbol{\tau} = \frac{\partial \Phi}{\partial \boldsymbol{\Delta}(\alpha, m_\alpha, \mathbf{r})} d(\alpha) = \frac{\pi \gamma(\alpha, m_\alpha)}{\mathbf{b}(\alpha, m_\alpha, \mathbf{r})} \sin\left[\frac{2\pi \boldsymbol{\Delta}(\alpha, m_\alpha, \mathbf{r})}{\mathbf{b}(\alpha, m_\alpha, \mathbf{r})}\right]. \tag{4}$$

The maximum shear stress defined as the interfacial shear strength is directly related to γ. The magnitude of the total interplanar slip is the sum of the inelastic slip and the elastic slip. At the glide plane, $\boldsymbol{\Delta}^{\mathrm{s}}$ has the form

$$\boldsymbol{\Delta}^{\mathrm{s}} = \mathbf{b}^{\mathrm{s}} \eta^{\mathrm{s}}(\mathbf{r}) + \frac{\pi d^{\mathrm{s}} \gamma^{\mathrm{s}}}{\mu \mathbf{b}^{\mathrm{s}}} \sin\left(\frac{2\pi \boldsymbol{\Delta}^{\mathrm{s}}}{\mathbf{b}^{\mathrm{s}}}\right), \tag{5}$$

and at the interface between phase I and II, $\boldsymbol{\Delta}^{\mathrm{int}}$ is given by

$$\boldsymbol{\Delta}^{\mathrm{int}} = \mathbf{b}^{\mathrm{int}} \eta^{\mathrm{int}}(\mathbf{r}) + \frac{\pi d^{\mathrm{int}} \gamma^{\mathrm{int}}}{\mu \mathbf{b}^{\mathrm{int}}} \sin\left(\frac{2\pi \boldsymbol{\Delta}^{\mathrm{int}}}{\mathbf{b}^{\mathrm{int}}}\right), \tag{6}$$

where the Burgers vector, the interplanar distance and the unstable SFE are $\mathbf{b}^{\mathrm{s}} = b[010]$, d^{s}, γ^{s} for the glide interface, and $\mathbf{b}^{\mathrm{int}} = b[010]$, d^{int}, γ^{int} for the interface, respectively. μ is the shear modulus of the system in the isotropic elasticity, $\gamma^{\mathrm{s}} = \gamma^{\mathrm{I}}$ in the phase I and $\gamma^{\mathrm{s}} = \gamma^{\mathrm{II}}$ in the phase II. Substituting Eqs. (3), (5), (6) into Eq. (2), the crystalline energy of the system becomes a functional of $\eta^{\mathrm{s}}(\mathbf{r})$ and $\eta^{\mathrm{int}}(\mathbf{r})$. Only in the limit of $d^{\mathrm{s}} = d^{\mathrm{int}} = 0$ under an unphysical condition, the term of the elastic slip in Eqs. (5),(6) disappears and the final expression of Eq. (2) reduces to that of the conventional crystalline energy function in terms of the inelastic slip [27]. Otherwise, the effect of the elastic slip cannot be ignored in particular during dislocation motion under an applied stress [44]. The elastic energy in Eq. (1) is mainly caused by the interplay between the external stress and the eigenstrain distribution from the inelastic slips. The eigenstrain $\varepsilon_{ij}^{0}(\mathbf{r})$ induced by the inelastic slips has the form

$$\varepsilon_{ij}^{0}(\mathbf{r}) = \frac{b_i^{\mathrm{s}} n_j^{\mathrm{s}}}{d^{\mathrm{s}}} \eta^{\mathrm{s}}(\mathbf{r}) + \frac{b_i^{\mathrm{int}} n_j^{\mathrm{int}}}{d^{\mathrm{int}}} \eta^{\mathrm{int}}(\mathbf{r}), \tag{7}$$

where n_j^{s} and n_j^{int} are the component of the unit normal vector of the glide plane and of the interface respectively. When the bi-material system is elastically homogeneous, the Khachaturyan-Shatalov theory [45,46] gives the exact solution of the elastic energy in terms of $\varepsilon_{ij}^{0}(\mathbf{r})$:

$$E^{elas}=\frac{1}{2}\int_{|\xi|\neq 0}\left[C_{ijkl}\tilde{\varepsilon}_{ij}^{0}(\xi)\tilde{\varepsilon}_{kl}^{0}(\xi)^{*}-e_i\tilde{\sigma}_{ij}^{0}(\xi)\Omega_{jk}(\mathbf{e})\tilde{\sigma}_{kl}^{0}(\xi)^{*}e_l\right]\frac{\mathrm{d}^3\xi}{(2\pi)^3}, \tag{8}$$

where C_{ijkl} is the elastic moduli tensor, ξ is the vector in the Fourier space, and $\mathbf{e}=\xi/|\xi|$ is the unit vector along ξ. $\tilde{\varepsilon}_{ij}^{0}(\xi)$ is the Fourier transformation of $\varepsilon_{ij}^{0}(\mathbf{r})$ given by the equation $\tilde{\varepsilon}_{ij}^{0}(\xi)=\int\varepsilon_{ij}^{0}(\mathbf{r},t)e^{-i\xi\cdot\mathbf{r}}d^3r$. $\tilde{\sigma}_{ij}^{0}(\xi)=C_{ijkl}\tilde{\varepsilon}_{kl}^{0}(\xi)$. $\Omega(\boldsymbol{e})_{jk}=\left(C_{jlpk}e_le_p\right)^{-1}$ is the elastic Green function, $\sigma_{ij}^{\mathrm{ext}}$ is the external applied stress and the symbol * denotes the complex conjugation. The integral $\int_{|\xi|\neq 0}$ is in the Fourier space excluding the points at $|\xi|=0$ and V is the total volume of the system. Substituting Eq. (7) into Eq.(8), the elastic energy of the system also becomes a functional of $\eta^{\mathrm{s}}(\mathbf{r})$ and $\eta^{\mathrm{int}}(\mathbf{r})$. The third term of Eq. (1) can be written as

$$E^{\mathrm{ext}}=-\int\sigma_{ij}^{\mathrm{ext}}\varepsilon_{ij}^{0}(\mathbf{r})\mathrm{d}^3r-\frac{V}{2}C_{ijkl}^{-1}\sigma_{ij}^{\mathrm{ext}}\sigma_{kl}^{\mathrm{ext}}, \tag{9}$$

After the total free energy is expressed as a function of the given two phase field variables, the variational derivatives of the total free energy with respect to $\left\{\eta^{\mathrm{s}}(\mathbf{r},t),\eta^{\mathrm{int}}(\mathbf{r},t)\right\}$ provide the driving forces for the evolution processes of $\left\{\eta^{\mathrm{s}}(\mathbf{r},t),\eta^{\mathrm{int}}(\mathbf{r},t)\right\}$ governed by the Ginzburg-Landau kinetic equations [27]:

$$\frac{\partial\left\{\eta^{\mathrm{s}}(\mathbf{r},t),\eta^{\mathrm{int}}(\mathbf{r},t)\right\}}{\partial t}=-L\frac{\delta E^{\mathrm{tot}}}{\delta\left\{\eta^{\mathrm{s}}(\mathbf{r},t),\eta^{\mathrm{int}}(\mathbf{r},t)\right\}}+\zeta(\alpha,m_\alpha,\mathbf{r},t), \tag{10}$$

where t is the time and L is the positive kinetic coefficient characterizing the relaxation rates of $\eta^{\mathrm{s}}(\mathbf{r})$ and $\eta^{\mathrm{int}}(\mathbf{r})$. $\zeta(\alpha,m_\alpha,\mathbf{r},t)$ is the Langevin Gaussian noise term mimicking thermal fluctuations. Substituting Eqs. (3), (8), (9) into Eq. (10), Eq.(10) can be rewritten as

$$\frac{\partial\eta^{\mathrm{s}}(\mathbf{r},t)}{\partial t}=-L\left[\frac{\pi\gamma^{\mathrm{s}}}{d^{\mathrm{s}}\mathbf{b}^{\mathrm{s}}}\sin\left(\frac{2\pi\boldsymbol{\Delta}^{\mathrm{s}}}{\mathbf{b}^{\mathrm{s}}}\right)\frac{\partial\boldsymbol{\Delta}^{\mathrm{s}}}{\partial\eta^{\mathrm{s}}}-\frac{\sigma_{ij}b_i^{\mathrm{s}}n_j^{\mathrm{s}}}{d^{\mathrm{s}}}\right]+\zeta(\alpha,m_\alpha,\mathbf{r},t), \tag{11.a}$$

$$\frac{\partial\eta^{\mathrm{int}}(\mathbf{r},t)}{\partial t}=-L\left[\frac{\pi\gamma^{\mathrm{int}}}{d^{\mathrm{int}}\mathbf{b}^{\mathrm{int}}}\sin\left(\frac{2\pi\boldsymbol{\Delta}^{\mathrm{int}}}{\mathbf{b}^{\mathrm{int}}}\right)\frac{\partial\boldsymbol{\Delta}^{\mathrm{int}}}{\partial\eta^{\mathrm{int}}}-\frac{\sigma_{ij}b_i^{\mathrm{int}}n_j^{\mathrm{int}}}{d^{\mathrm{int}}}\right]+\zeta(\alpha,m_\alpha,\mathbf{r},t), \tag{11.b}$$

where $\sigma_{ij}=\sigma_{ij}^{\mathrm{ext}}+C_{ijkl}\left[\bar{\varepsilon}_{kl}^{0}+\frac{1}{2}\int_{|\xi|\neq 0}\frac{\left(e_k\Omega_{li}+e_l\Omega_{ki}\right)\tilde{\sigma}_{ij}^{0}e_j\,e^{i\xi\cdot\mathrm{r}}}{(2\pi)^3}d^3\xi-\varepsilon_{kl}^{0}\right]$ is the elastic stress with

$\bar{\varepsilon}_{kl}^{0}=\frac{1}{V}\int\varepsilon_{ij}^{0}(\mathbf{r},t)d^{3}r$. After the spatial length is in unit 0.25b and the time is in unit $t_c=1/(L\mu)$, the reduced forms of Eq.(11) are governed by the given dimensionless parameters: $d^{\text{int}}/b=1$, $d^{\text{s}}/b=1$, $\bar{\gamma}^{\text{A}}=\gamma^{\text{A}}/\left(\frac{\mu b}{2\pi^{2}}\right)$ with A=s, int, and $\bar{\sigma}_{ij}^{\text{exit}}=\sigma_{ij}^{\text{exit}}/\mu$. In the simulations, using a finite difference method, Eqs. (11.a) and (11.b) are solved in the computational cell $512\times4\times512$ with periodic boundary conditions along all three dimensions to give the time evolution of the slip profiles at the glide plane and the interface under applied stress. An artificial weak interface with $\bar{\gamma}^{\text{s}}=0$ is assumed at $x=256$ to adsorb the image glide dislocation. The steady solutions of Eq. (11) further give the equilibrium configuration corresponding to $\delta E^{\text{tot}}/\delta\left\{\eta^{\text{s}}(\mathbf{r},t),\eta^{\text{int}}(\mathbf{r},t)\right\}=0$. After the profile of $\eta^{\text{s}}(\mathbf{r})$ is calculated, the core width w^{s} and the position X^{s} of the glide dislocation can be estimated by

$$w^{\text{s}}=\left|x\right|_{\eta^{\text{s}}=0.75}-x\left|_{\eta^{\text{s}}=0.25}\right| \tag{12}$$

and

$$X^{\text{s}}=\int_{0}^{1}x\left(\eta^{\text{s}}\right)d\eta^{\text{s}}. \tag{13}$$

If the total energy is a function of the position of the glide dislocation, the negative derivative of the total free energy with respect to X^{s} generates the configurational force on the glide dislocation. Negative configurational force acts as resistant force for the movement of the glide dislocation and vice versa. The following numerical results will show the changes of $\eta^{\text{s}}(\mathbf{r})$ and $\eta^{\text{int}}(\mathbf{r})$ during the glide dislocation transmission across the interface under different levels of applied shear stress by varying the interfacial shear strength, as well as the associated changes of the total energy and the configurational force on the glide dislocation.

3. Results and Discussion

The interfacial barrier to glide dislocation slip transmission is influenced by both the dislocation core changes and the cross-slip interaction between the glide dislocation and induced interfacial dislocations. The results consist of two sub-sections. In Section 3.1, the interface is assumed to be strongly bonded so that it is non-shearable, and the effect of the SFE mismatch on the dislocation core change as well as the interface resistance is investigated. In Section 3.2, the interface with weak interfacial bonding can be sheared by the stress field of the glide dislocation and the influence of the interface shear on the interfacial barrier is studied.

3.1. The interfacial resistance of a non-shearable interface

If the interface is non-shearable, $\bar{\gamma}^{\text{int}}$ is viewed as infinite and we assumed $\eta^{\text{int}}(\mathbf{r},t)\equiv 0$. For a bi-material system with the given SFE mismatch characterized by $\bar{\gamma}^{\text{I}}=1.0$, $\bar{\gamma}^{\text{II}}=0.2$, Figure 2 shows the change of the core width of the glide dislocation decreases rapidly during its transmission across the interface from phase II to phase I under the external shear $\sigma_{yz}^{\text{ext}}/\mu=0.021$. The change of the line is piece-wise in this figure, because the minimum resolution for the core width determined by Eq. (12) is the spatial length 0.25*b*. This trend of the core width change is consistent with the known predicting $w^s/b\sim 1/\bar{\gamma}^s$ in elastic homogenous phases [14].

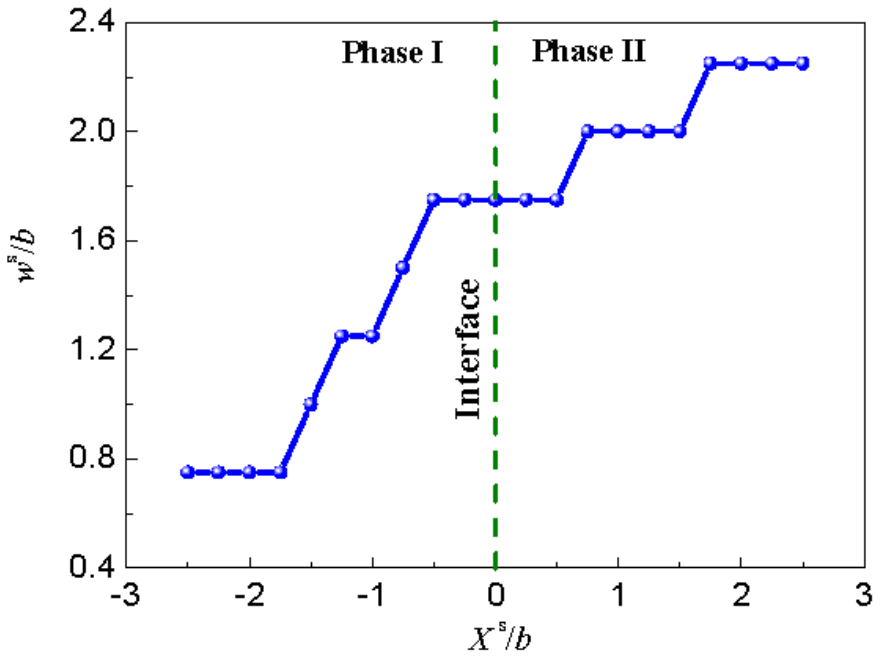

Figure 2. The core width w^s of the glide dislocation plotted as a function of its position X^s during its transmission across the bimaterial interface without interface shear under given parameters $\bar{\gamma}^{\text{I}}=1.0$, $\bar{\gamma}^{\text{II}}=0.2$ and $\sigma_{yz}^{\text{ext}}/\mu=0.021$.

The rapid decrease of the core width near the interface would cause large energy change of the system during the transmission process. Figure 3 plots the energy change with respect to the position of the glide dislocation when it spontaneously moves from phase I to phase II with $\bar{\gamma}^{\text{I}}=1.0$, $\bar{\gamma}^{\text{II}}=0.2$ in the absence of applied stress. Therefore the negative derivative of the energy with respect to the position of the glide dislocation generates a resistance force for the transmission of the glide dislocation from phase II to phase I. This resistance force is originated from the energy change of the

dislocation core change due to the SFE mismatch between the two phases. Figure 4 plots the profile of $\eta^s(x)$ with respect to x/b at the glide plane under different levels of applied shear stress under given parameters $\bar{\gamma}^{\mathrm{I}}$=1.0 and $\bar{\gamma}^{\mathrm{II}}$=0.2. The results show that the glide dislocation can slip transmission over the interface from phase II to phase I only if the applied stress exceeds a critical value. This critical applied stress, $\sigma_{yz}^{\mathrm{ext}}/\mu$=0.021, is equal to the maximum resistant force that should be overcome during the dislocation transmission across the interface and is defined as the interfacial barrier strength τ^*.

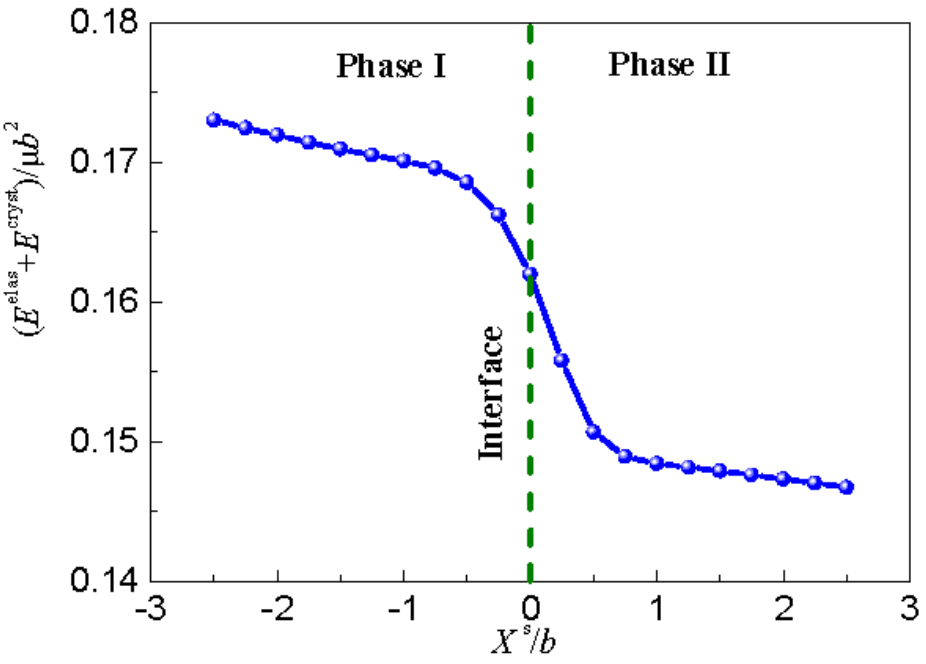

Figure 3. Plot of the dislocation free energy E^{tot} as a function of the position of the glide dislocation X^s in the absence of applied shear stress without interface shear under the given parameters $\bar{\gamma}^{\mathrm{I}}$=1.0 and $\bar{\gamma}^{\mathrm{II}}$=0.2.

According to the definition of the interfacial barrier strength in Figure 4, the interfacial barrier strengths without interface shear are calculated for different $\bar{\gamma}^{\mathrm{I}}$ and $\bar{\gamma}^{\mathrm{II}}$. Figure 5 shows τ^* increases linearly with difference $\Delta\bar{\gamma}=\bar{\gamma}^{\mathrm{I}}-\bar{\gamma}^{\mathrm{II}}$ and is insensitive to the average $\bar{\gamma}_{\mathrm{avg}}=\left(\bar{\gamma}^{\mathrm{I}}+\bar{\gamma}^{\mathrm{II}}\right)/2$. The calculated result is consistent with the analytic solution given by Anderson and Xin [14] in the case of no elastic mismatch. These results demonstrate that the larger SFE mismatch induces the larger dislocation core change during the transmission process and causes more rapid change of the dislocation energy near the interface, and leads to larger interfacial resistance.

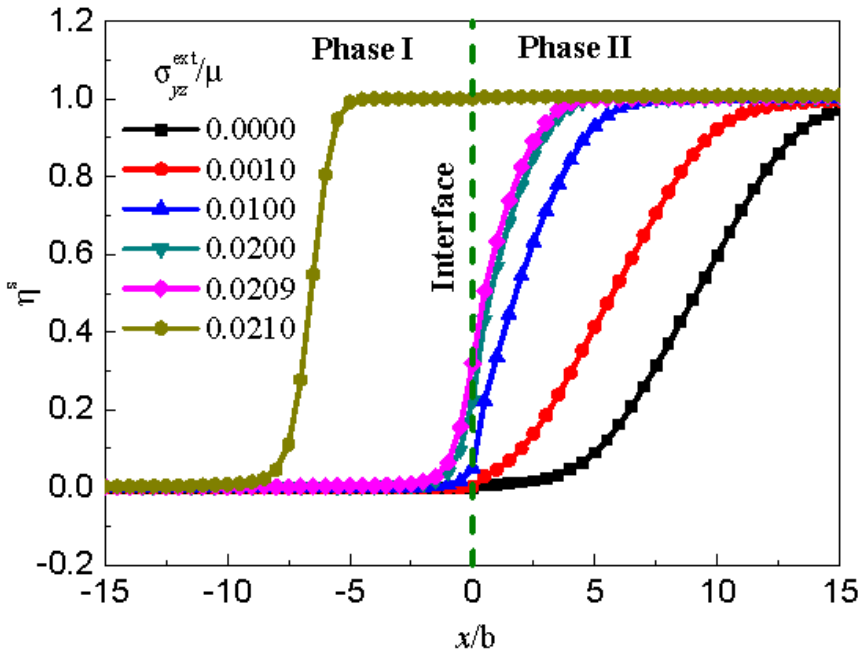

Figure 4. The profile of $\eta^s(\mathbf{r},t)$ plotted with respect to x/b at the glide plane under different levels of applied shear stress without interface shear under the given parameters $\bar{\gamma}^{\mathrm{I}}=1.0$ and $\bar{\gamma}^{\mathrm{II}}=0.2$.

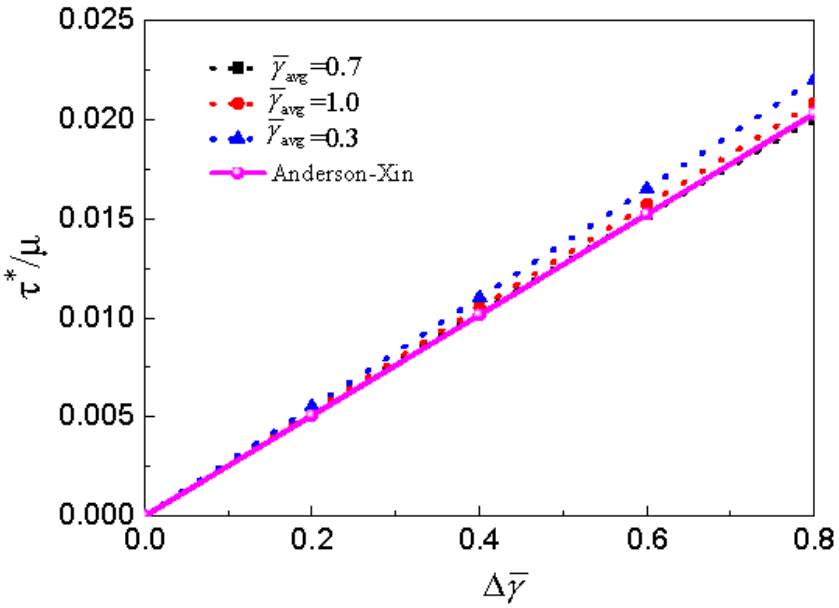

Figure 5. Plot of the calculated interfacial barrier strength without interface shear as a function of $\Delta\bar{\gamma}$ and $\bar{\gamma}_{\mathrm{avg}}$ in comparison with the analytic solution given by Anderson and Xin [34].

3.2. Influence of the interface shear on the interfacial resistance

When the interface has limited shear strength and it could be sheared by the stress field of the glide dislocation. To investigate the effects of interface shear, we keep $\bar{\gamma}^{\mathrm{I}}=\bar{\gamma}^{\mathrm{II}}=1.0$ and only vary the value of $\bar{\gamma}^{\mathrm{int}}$**.** The distribution of normalized interfacial shear stress σ_{xy}/μ plotted with respect to z/b at the interface in Figure 6 clearly shows that the interface shearing could effectively counteract the shear stress concentration induced by the glide dislocation at the interface under the given parameters $\bar{\gamma}^{\mathrm{I}}=\bar{\gamma}^{\mathrm{II}}=1.0$ and $\sigma_{yz}^{\mathrm{ext}}/\mu=0$. Figs. (7), (8), plot the profiles of $\eta^{s}(x)$ and $\eta^{\mathrm{int}}(z)$, respectively, under different levels of applied shear stress with the given parameters $\bar{\gamma}^{\mathrm{I}}=\bar{\gamma}^{\mathrm{II}}=1.0$ and $\bar{\gamma}^{\mathrm{int}}=0.2$. Figure 7 shows that the glide dislocation cannot transmit across the interface until the external shear stress is up to a critical value. After $\sigma_{yz}^{\mathrm{ext}}/\mu\geq 0.0277$, the glide dislocation can slip across the interface, it indicates that the interface barrier strength is $\tau^{*}=0.0277\mu$. In comparison with $\tau^{*}=0$ in the similar case without interface shear as simulated in Figure 5, we believe that it is the interface shear leading to the significant increase of τ^{*}, which is consistent with the previous results of atomistic simulation and modeling [21–25]. From Figure 7, the dislocation core is constricted heavily when it reaches the interface. The reason is that the interface shear can reduce the elastic energy by counteracting the shear stress, the dislocation core tends to be trapped and constricted onto the sharp interface to relieve the elastic energy.

The interface shearing at the interface results in an inelastic shear zone via nucleation and growth of interfacial dislocations. Figure 8 shows that the inelastic shear zone is noticeable when the glide dislocation is trapped at the interface under $\sigma_{yz}^{\mathrm{ext}}/\mu=0.001$, it subsequently shrinks and disappears as the increased external shear stress is up to $\sigma_{yz}^{\mathrm{ext}}/\mu=0.0277$ consistent with the glide dislocation away from the interface. It is worth to note that when the glide dislocation is trapped at the interface, there are oscillations on the profiles of the field variables as shown in Figure 7 and 8. The reason is that we use the periodic Fast Fourier Transformation to solve the elastic filed of the almost singular glide dislocation trapped in the sharp interface, and these unphysical oscillations can be mitigated when the interface is treated as diffuse. The calculated sequential contour-maps of the profiles of $\eta^{s}(\mathbf{r},t)$ and $\eta^{\mathrm{int}}(\mathbf{r},t)$ during the glide dislocation transmission is shown in Figure 9. The snapshots in Figure 9 clearly show that the inelastic shear zone adaptively changes through the reversible movement of the interfacial dislocation driven by the stress field of the glide dislocation close to or away from the interface.

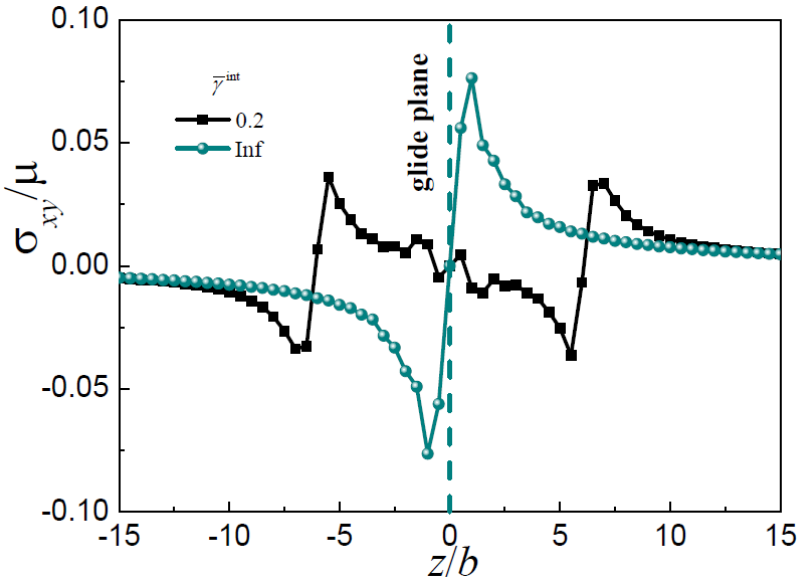

Figure 6. The distribution of normalized interfacial shear stress σ_{xy}/μ plotted with respect to z/b at the interface with interface shear ($\bar{\gamma}^{\text{int}}=0.2$) and without interface shear ($\bar{\gamma}^{\text{int}}=\text{Inf}$) when the glide dislocation is trapped at the interface in the absence of applied shear stress under the given parameters $\bar{\gamma}^{\text{I}}=\bar{\gamma}^{\text{II}}=1.0$.

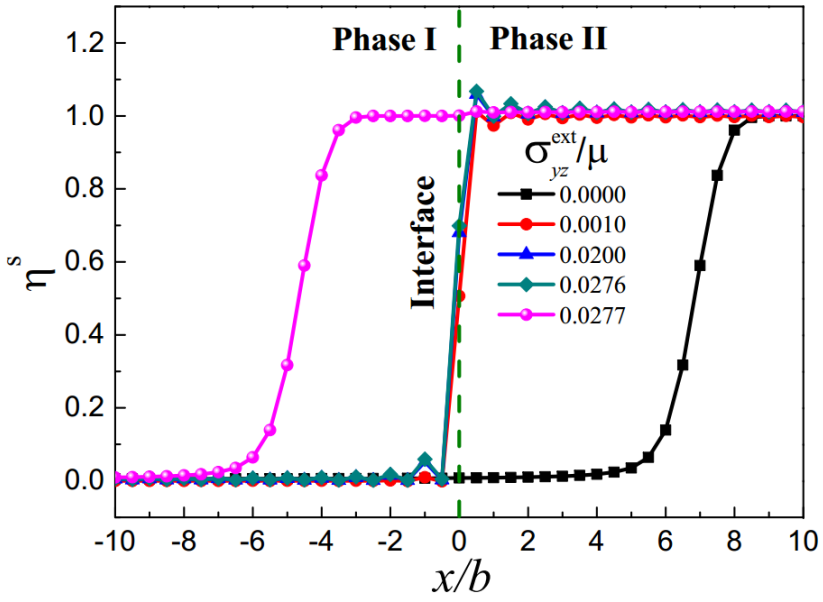

Figure 7. The profile of $\eta^s(\mathbf{r},t)$ plotted with respect to x/b at the glide plane under different levels of applied shear stress under the given parameters $\bar{\gamma}^{\text{I}}=\bar{\gamma}^{\text{II}}=1.0$ and $\bar{\gamma}^{\text{int}}=0.2$.

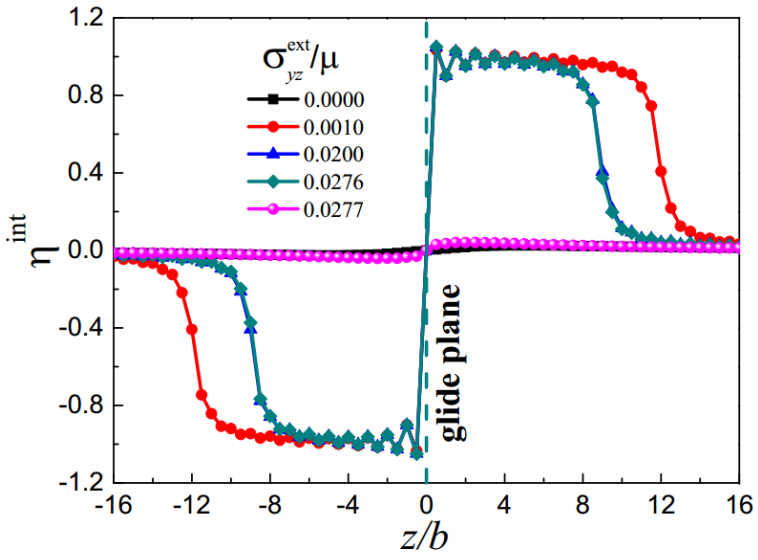

Figure 8. The profile of $\eta^{\text{int}}(\mathbf{r},t)$ plotted with respect to z/b at the interface under different levels of applied shear stress under the given parameters $\bar{\gamma}^{\text{I}}=\bar{\gamma}^{\text{II}}=1.0$ and $\bar{\gamma}^{\text{int}}=0.2$.

Figure 10 plots the profile of $\eta^{\text{int}}(z)$ under different values of $\bar{\gamma}^{\text{int}}$ when the glide dislocation is trapped at the interface in the absence of applied shear stress under the given parameters $\bar{\gamma}^{\text{I}}=\bar{\gamma}^{\text{II}}=1.0$. The results in Figure 10 show that a wider inelastic shear zone is developed for the interface with a lower shear strength. We performed numerical simulations for the glide dislocation transmission across the interface with different interfacial shear strength under external shear stress. Figure 11 plots the simulated interfacial barrier strength as a function of $\bar{\gamma}^{\text{int}}$ under the given parameters $\bar{\gamma}^{\text{I}}=\bar{\gamma}^{\text{II}}=1.0$. It is found that the interfacial barrier strength significantly increases as the value of $\bar{\gamma}^{\text{int}}$ is lower than 0.8. When the value of $\bar{\gamma}^{\text{int}}$ is larger than 0.8, the interfacial barrier strength reaches a minimum (zero), which is the same as the prediction in the case without interface shear. Herein the enhancement of the interfacial barrier strength due to the interface shearing is neglectable. This is because the inelastic shear zone almost disappears at $\bar{\gamma}^{\text{int}}=0.8$ as indicated in Figure 10. These results reproduce some atomistic simulations trends revealing the "weak" interface strengthening mechanism [25].

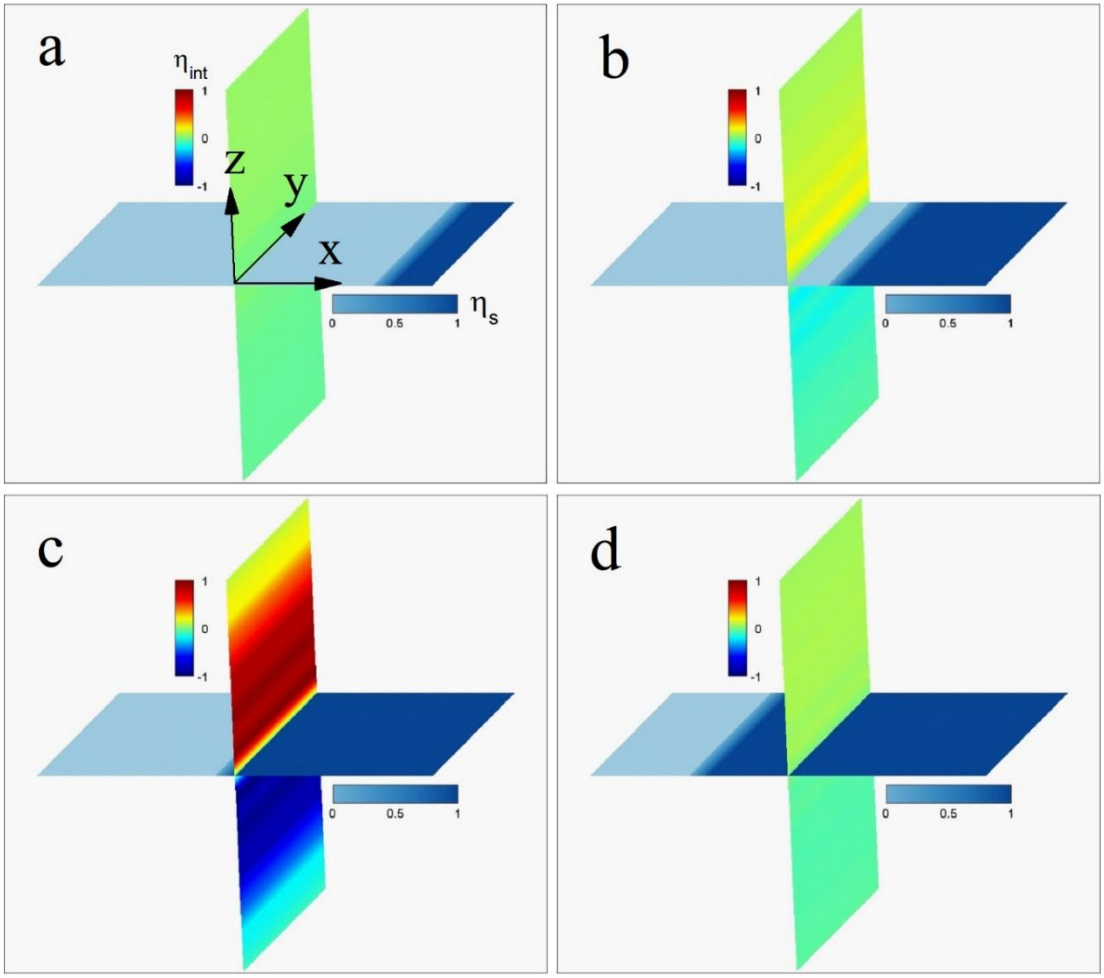

Figure 9. The simulated snapshots of the profile of $\eta^s(\mathbf{r},t)$ and $\eta^{int}(\mathbf{r},t)$ under the given parameters $\bar{\gamma}^{I}=\bar{\gamma}^{II}=1.0$, $\bar{\gamma}^{int}=0.2$ and $\sigma_{yz}^{ext}/\mu=0.0277$. The snapshots are captured when the glide dislocation is (a) initially in phase II, (b) approaching the interface, (c) trapped at the interface and (d) in phase I after transmission across the interface.

The resistant force of the glide dislocation with interface shearing is originated from the increase of the total free energy as the glide dislocation away from the interface. Figure 12 plots the elastic energy E^{elas} and crystalline energy E^{cryst} as a function of the position of the glide dislocation X^s for $\bar{\gamma}^{int}=0.2$ and $\bar{\gamma}^{int}=0.8$ in the absence of applied shear stress. Both E^{elas} and E^{cryst} decrease when the glide dislocation is close to the interface. The interface involving interface shearing acts as an energy well, which can trap the glide dislocation at the interface. The energy well for $\bar{\gamma}^{int}=0.2$ is deeper and narrower than that for $\bar{\gamma}^{int}=0.8$. The deeper the energy well at the interface, the larger the attractive force on the glide dislocation, and the higher the interfacial barrier strength. The results in Figure 12 indicate that the attractive force is attributed to not only the elastic

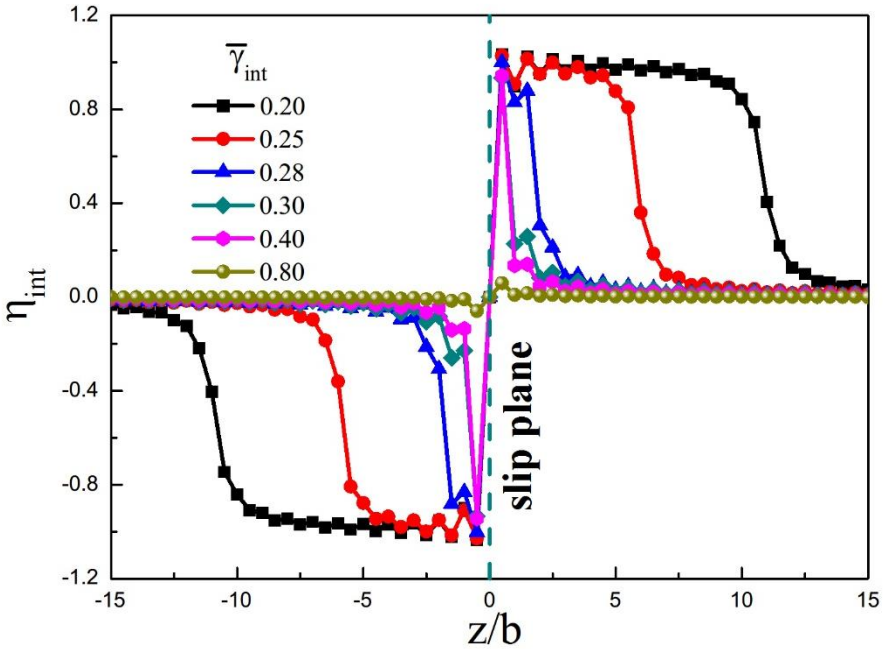

Figure 10. The profile of $\eta^{\text{int}}(\mathbf{r},t)$ plotted with respect to z/b at the interface with different values of $\overline{\gamma}^{\text{int}}$ when the glide dislocation is trapped in the interface in the absence of applied shear stress under the given parameters $\overline{\gamma}^{\text{I}}=\overline{\gamma}^{\text{II}}=1.0$.

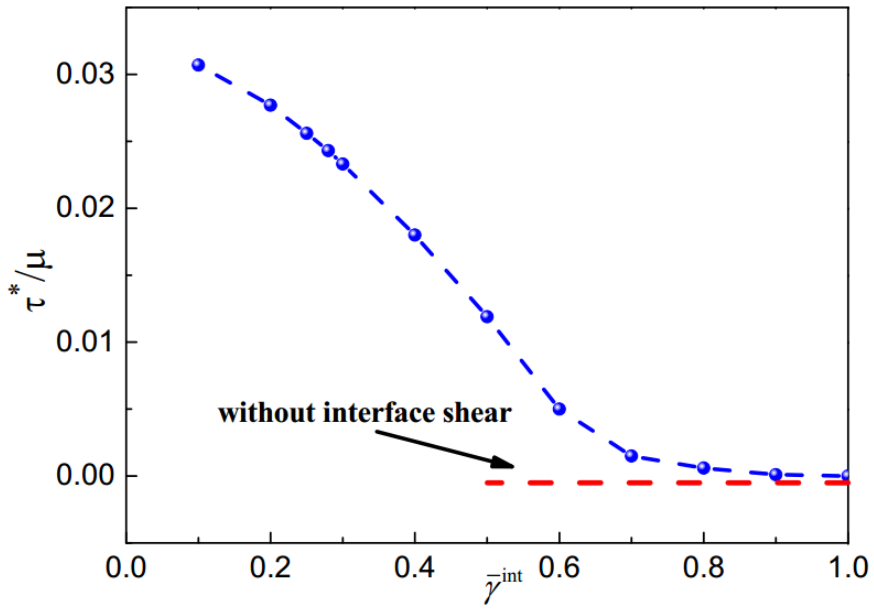

Figure 11. Plot of the calculated interfacial barrier strength τ^* as a function of $\overline{\gamma}^{\text{int}}$ under the given parameters $\overline{\gamma}^{\text{I}}=\overline{\gamma}^{\text{II}}=1.0$. Dashed line shows the interfacial barrier strength without interface shear.

interaction between the glide dislocation and interfacial dislocation [12,18] but also the crystalline energy change due to the core-width change of the dislocations [16]. At the continuum scale, the dislocation core change is usually ignored in the dislocation-based models [12,18]. In such situation the resistant force on the glide dislocation is only related to the change of the elastic energy and therefore is underestimated. The current simulation results show that the change of the dislocation crystalline energy induced by the core change also has large contribution to the interfacial barrier strength, especially for the weak interface.

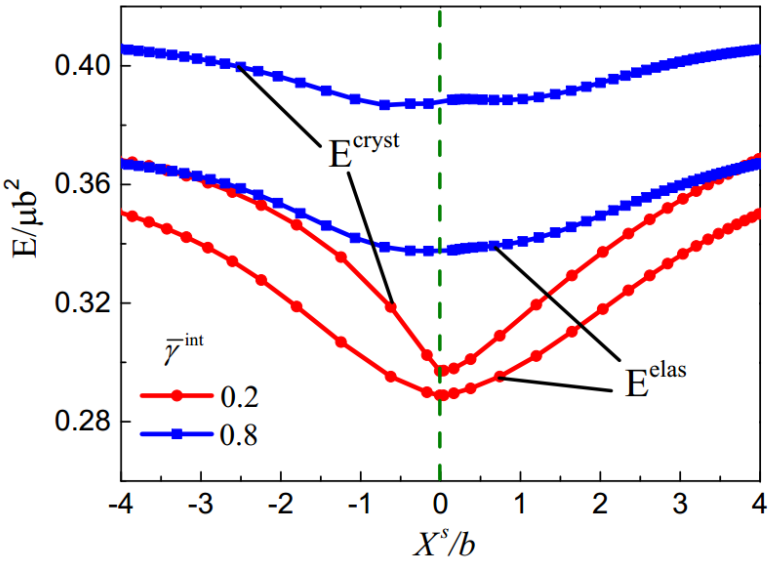

Figure 12. Plots of the elastic energy E^{elas} and crystalline energy E^{cryst} as a function of the position of the glide dislocation X^s for $\bar{\gamma}^{int}=0.2$ and $\bar{\gamma}^{int}=0.8$ in the absence of applied shear stress under the given parameters $\bar{\gamma}^{I}=\bar{\gamma}^{II}=1.0$.

4. Conclusions

In summary, 3D PFM modeling and simulation are adopted to investigate a glide dislocation transmission across a coherent sliding interface. The interfacial barrier strength for the transmission is investigated with and without interface shear. In the case without interface shear, the resistant force on the glide dislocation across the interface mainly depends on the core-width change induced by the SFE mismatch, which is in good agreement with the theoretical solutions. In the case with interface shear, we show that weak interface develops a wide inelastic shear zone under the stress field of the glide dislocation, and can exert a large attractive force on the glide dislocation and thus largely enhance the interfacial barrier strength. The attractive force is attributed to both the elastic interaction between the glide dislocation and interfacial dislocation and the core change of them. The continuum model for the dislocation transmission across the weak interface without the core-width change may significantly underestimate the interfacial barrier strength.

Acknowledgments

This work was supported by the Basic Research Program of China (Grant No. 2011CB302100) and the National Natural Science Foundation of China (Grant No. 11222219, 11132009).

Conflict of Interest

The authors declare no conflicts of interest in this paper.

References

1. Argon AS (2008) *Strengthening mechanisms in plasticity.* Oxford: Oxford University Press.
2. Kubin LP (2013) *Dislocations, mesoscale simulations and plastic flow.* Oxford: Oxford University Press.
3. Bulatov VV, Cai W (2006) *Computer simulations of dislocations.* Oxford: Oxford University Press.
4. Arzt E (1998) Size effects in materials due to microstructural and dimensional constraints: a comparative review *Acta Mater* 46: 5611–5626.
5. Misra A, Kung H (2001) Deformation behavior of nanostructured metallic multilayers *Adv Eng Mater* 3: 217–222.
6. Lu K, Lu L, Suresh S (2009) Strengthening materials by engineering coherent internal boundaries at the nanoscale. *Science* 324: 349–352.
7. Misra A, Hirth JP, Hoagland RG (2005) Length-scale-dependent deformation mechanisms in incoherent metallic multilayered composites. *Acta Mater* 53: 4817–4824.
8. Wang J, Misra A (2011) An overview of interface-dominated deformation mechanisms in metallic multilayers. *Curr Opin Solid State Mater Sci* 15: 20–28.
9. Misra A, Hirth JP, Kung H (2002) Single-dislocation-based strengthening mechanisms in nanoscale metallic multilayers. *Phil Mag A* 82: 2935–2951.
10. Anderson PM, Foecke T, Hazzledine PM (1999) Dislocation-based deformation mechanisms in metallic nanolaminates. *MRS Bull* 24: 27–33.
11. Clemens BM, Kung H, Barnett SA (1999) Structure and strength of multilayers. *MRS Bulletin* 24: 20–26.
12. Hoagland RG, Mitchell TE, Hirth JP, et al. (2002) On the strengthening effects of interfaces in multilayer fee metallic composites. *Phil Mag A* 82: 643–664.
13. Li QZ, Anderson PM (2005) Dislocation-based modeling of the mechanical behavior of epitaxial metallic multilayer thin films. *Acta Mater* 53: 1121–1134.
14. Anderson PM, Xin X (2000) The Critical Shear Stress to Transmit A Peierls Screw Dislocation Across A Non-slipping Interface. *Multiscale Fracture and Deformationin Materials and Structures: The James R Rice 60th Anniversary Volume.* Springer Netherland; 84: 87–105.
15. Anderson PM, Li Z (2001) A Peierls analysis of the critical stress fortransmission of a screw dislocation across a coherent, sliding interface. *Mater Sci Eng A* 319:182–187.
16. Shen Y, Anderson PM (2006) Transmission of a screw dislocation across acoherent, slipping interface. *Acta Mater* 54: 3941–3951.

17. Shen Y, Anderson PM (2007) Transmission of a screw dislocation across a coherent, non-slipping interface. *J Mech Phys Solids* 55: 956–979.
18. Chu HJ, Wang J, Beyerlein IJ, et al. (2013) Dislocation models of interfacial shearing induced by an approaching lattice glide dislocation. *Int J Plast* 41: 1–13.
19. Demkowicz MJ, Wang J, Hoagland RG (2008) Interfaces between dissimilar crystalline solids. *Dislocations in Solids*. Amsterdam: Elsevier North-Holland; 14: 141–205.
20. Rao SI, Hazzledine PM (2000) Atomistic simulations of dislocation–interface interactions in the Cu-Ni multilayer system. *Phil Mag A* 80: 2011–2040.
21. Hoagland RG, Hirth JP, Misra A (2006) On the role of weak interfaces in blocking slip in nanoscale layered composites. *Phil Mag* 86: 3537–3558.
22. Wang J, Hoagland RG, Hirth JP, et al. (2008) Atomistic modeling of the interaction of glide dislocations with "weak" interfaces. *Acta Mater* 56: 5685–5693.
23. Wang J, Hoagland RG, Hirth JP, et al. (2008) Atomistic simulations of the shear strength and sliding mechanisms of copper–niobium interfaces. *Acta Mater* 56: 3109–3119.
24. Wang J, Hoagland RG, Liu XY, et al. (2011) The influence of interface shear strength on the glide dislocation–interface interactions. *Acta Mater* 59: 3164–3173.
25. Wang J, Misra A, Hoagland RG, et al. (2012) Slip transmission across fcc/bcc interfaces with varying interface shear strengths. *Acta Mater* 60: 1503–13.
26. Zhu T, Li J, Samanta A, et al. (2007) Interfacial plasticity governs strain rate sensitivity and ductility in nanostructured metals. *Proc Natl Acad Sci* 104: 3031–3036.
27. Wang YU, Jin YM, Cuitino AM, et al. (2001) Nanoscale phase field microelasticity theory of dislocations: model and 3D simulations. *Acta Mater* 49:1847–1857.
28. Wang Y, Li J (2010) Phase field modeling of defects and deformation. *Acta Mater* 58: 1212–1235.
29. Shen C, Wang Y (2003) Phase field model of dislocation networks. *Acta Mater* 51: 2595–2610.
30. Shen C, Wang Y (2004) Incorporation of γ-surface to phase field model of dislocations: simulating dislocation dissociation in fcc crystals. *Acta Mater* 52: 683–691.
31. Koslowski M, Cuitino AM, Ortiz M (2002) A phase-field theory of dislocation dynamics, strain hardening and hysteresis in ductile single crystals. *J Mech Phys Solids* 50: 2597–2635.
32. Hunter A, Beyerlein IJ, Germann TC, et al. (2011) Influence of the stacking fault energy surface on partial dislocations in fcc metals with a three-dimensional phase field dislocations dynamics model. *Phys Rev B* 84: 144108.
33. Koslowski M, Lee DW, Lei L (2011) Role of grain boundary energetics on the maximum strength of nanocrystalline Nickel. *J Mech Phys Solids*, 59: 1427–1436.
34. Cao L, Hunter A, Beyerlein IJ, et al. (2015) The role of partial mediated slip during quasi-static deformation of 3D nanocrystalline metals. *J Mech Phys Solids* 78:415–426.
35. Mianroodi JR, Svendsen B (2015) Atomistically determined phase-field modeling of dislocation dissociation, stacking fault formation, dislocation slip, and reactions in fcc systems. *J Mech Phys Solids* 77: 109–122.
36. Zheng SL, Ni Y, He LH (2015) Phase field modeling of a glide dislocation transmission across a coherent sliding interface. *Modelling Simul Mater Sci Eng* 23: 035002.
37. Vitek V (1968) Intrinsic stacking faults in body-centred cubic crystals. *Phil Mag* 18: 773–786
38. Levitas VI, Javanbakht M (2012) Advanced phase-field approach to dislocation evolution. *Phys.Rev B*86: 140101.

39. Levitas VI, Javanbakht M (2013) Phase field approach to interaction of phase transformation and dislocation evolution. *Appl Phys Lett* 102: 251904.
40. Levitas VI, Javanbakht M (2014) Phase transformations in nanograin materials under high pressure and plastic shear: nanoscale mechanisms. *Nanoscale* 6: 162–166.
41. Levitas VI, Javanbakht M (2015) Thermodynamically consistent phase field approach to dislocation evolution at small and large strains. *J Mech Phys Solids* 82: 345–366.
42. Levitas VI, Javanbakht M (2015) Interaction between phase transformations and dislocations at the nanoscale Part 1 General phase field approach. *J Mech Phys Solids* 82: 287–319.
43. Levitas VI, Javanbakht M (2015) Interaction between phase transformations and dislocations at the nanoscale Part 2 Phase field simulation examples. *J Mech Phys Solids* 82: 164–185.
44. Rice JR (1992) Dislocation nucleation from a crack tip: an analysis based on the Peierls concept. *J Mech Phys Solids* 40: 239–271.
45. Khachaturyan AG, Shatalov GA (1969) Elastic interaction potential of defects in a crystal. *Sov Phys Solid State* 11: 118–123.
46. Khachaturyan AG (1982) *Theory of structural transformations in solids*. New York: John Wiley & Sons.

AIMS Press